Document en libre accès dans PolyPublie
Open Access document in PolyPublie

Document publié chez l'éditeur officiel
Document issued by the official publisher

Ce fichier a été téléchargé à partir de PolyPublie, le dépôt institutionnel de Polytechnique Montréal
This file has been downloaded from PolyPublie, the institutional repository of Polytechnique Montréal

https://publications.polymtl.ca

An Active Dead-Time Control Circuit With Timing Elements for a 45-V Input 1-MHz Half-Bridge Converter

Mousa Karimi, *Member, IEEE*, Mohamed Ali, *Member, IEEE*, Ahmad Hassan, *Member, IEEE*, Mohamad Sawan, *Fellow, IEEE*, and Benoit Gosselin, *Member, IEEE*

Abstract—In this study, a dead-time control circuit is proposed to generate independent delays for the high and low sides of half-bridge converter switches. In addition to greatly decreasing the losses of power converters, the proposed method mitigates the shoot-through current through the application of superimposed power switches. The circuit presented here comprises a switched capacitor architecture and is implemented in AMS 0.35 μm technology. In the implementation, the proposed dead-time control circuit occupies a silicon area of 70 μm × 180 μm. To realize the technique, a two-sided wide swing current source is employed. Each sides of the current source comes with two capacitors, two Schmitt triggers, and three transmission gates. Results show that the low and high sides of the projected half-bridge converter switches respectively require delays of 35 and 62 ns. The performance of the proposed dead-time circuit is evaluated by assembling it with the half-bridge converter. The proposed dead-time prototype achieves a 40% drop in power losses in the half-bridge circuit.

Index Terms—Power management, half-bridge, switched capacitors, dead-time control circuit, power losses, power converters, shoot-through.

I. INTRODUCTION

DIFFERENT applications require various types of power converters, including DC–DC boost/buck converters [1]–[3], class-D power amplifiers [4], half-bridge converters [5], and switched-capacitor circuits [6]. These converters are mainly applied to system basis chips in automation, including those used in airbag squib drivers, braking valve drivers, and power steering integrated circuits [7]–[10]. Power converters are also widely used in neural stimulation and wireless power transmission in implantable biomedical microsystems [11]–[14].

Dense and miniaturized power converters comprising small passive components are useful in high-frequency application, but the switching losses of power switches limit the operating frequency of these devices [15]–[17]. In addition to switching losses, power converters suffer from conduction and gate charge losses that affect their efficiency [18], [19]. Their safety also tends to be affected by power switches' false or immature ON-state [20]. These drawbacks are mainly attributed to the parasitic inductances and capacitances of power switches [21]. A half-bridge output stage is shown in Fig. 1 along with the equivalent circuit of a power switch with the associated parasitic inductance. The figure also demonstrates the power switch's input capacitance (C_{iss}), output capacitance (C_{oss}), and reverse transfer capacitance (C_{rss}). These elements cause electromagnetic interferences and parasitic oscillations and are thus undesirable [22].

In implementing gate drivers, several techniques are used to accelerate the charge/discharge of unwanted elements of C_{iss} and C_{oss} and to mitigate the switching and gate charge losses of power switches. A soft-switching technique was proposed in [6], [23], [24] to reduce switching losses. The resonant gate driver approach is also widely used to reduce gate charge losses [25]. In [20], a specific double-pulse test was conducted to study the hard switching of power switches. Moreover, the high-voltage energy storing (HVES) approach was utilized to increase the gate driving speed [26]. In the HVES methodology, the authors aimed to decrease the adverse effects of parasitic gate loop inductance by embedding an on-chip resonant LC tank.

Standard high-voltage automotive data buses often require operating voltage from -27V to +45V to drive hydraulic actuators with power converters [27]. The power converters mainly operate with dead-time control circuits (DTCCs) [28]. These circuits have two main structures. Logic gates are sometimes used to create delays and thereby implement a dead-time between the activation of complementary conductive paths and avoid overlap [20], [29]–[31]. In other cases, time constants are used and implemented with resistors, capacitors, current

sources, etc. [32]. The latter is preferred for high voltage applications that require long delays [33]. In the use of logic gates, a fixed circuit that is not changed during operation is typically implemented. In the use of time constants, the controlling signals and switching techniques should be regulated to control the current source and capacitors and thereby create the dead-time.

A set of two superimposed complementary power switches makes up a power converter [34]. Half-bridge converters, in particular, utilizes two superimposed complementary power switches as the output stage to drive a given load (Fig. 2(a)). Most of the power budget in a half-bridge circuit is consumed in the output stage, during which shoot-through and losses occur. Shoot-through arises when two power switches are inadvertently closed at the same time, thereby causing unnecessary power losses and potential damages [35]. Such phenomenon can be avoided by creating a dead-time interval between the control signals of power switches [36]. Figure 2(a) shows the circuit of a half-bridge convertor, including a dead-time part, gate driver, high-side power switch (HSPS), and low-side power switch (LSPS). Figure 2(b) shows that in the scenario in which one of the superimposed complementary switches is turned on before or while the other switch is turned off, a shoot-through current can flow from the supply rail to the ground during the overlap time interval. In this case, non-overlapping driving signals should be provided to the power switches via a DTCC [37].

Shoot-through may also result from ringing in the driving circuit; such phenomenon increases the gate-to-source voltage (V_{GS}) of the high-side switches above the threshold voltage (V_{TH}) of the power transistor (Fig. 2(c)) [38]. This issue is commonly observed in gallium nitride (GaN) high electron mobility transistors (HEMTs) because of their low V_{TH} ($\sim$1 V) [39] relative to other types of power switches, such as silicon carbide and conventional silicon (V_{TH} of $\sim$2.5 V) [40]. This property of GaN HEMTs is attributable to the output parasitic capacitance (C_{oss}) of the high-side power switch. GaN HEMTs are commonly applied to power converters because of their various advantages, including their low on-resistance and parasitic capacitance, high operating temperature, and small package size. Furthermore, small junction capacitance, lack of body diode, and no reverse recovery loss are three advantages of GaN transistors over Si or SiC MOS. While, in the Si or SiC MOS, in addition to reverse recovery, there is also forward bias losses (V_F) of the body diode.

As for the ringing effect in the driving circuit, the issue can be addressed by adjusting the damping ratio or by providing enough dead-time interval between the driving signals of complementary switches. The transient response of the main switching circuit can cause the formation of Miller capacitance at the gate of the low-side complementary switch. This condition results in the VGS of the switches to exceed V_{TH} (Fig. 2(d)). In this scenario, the switching frequency of the circuit should be fine-tuned to handle the high dv/dt and di/dt without exceeding V_{TH} [41]. Non-overlapping signal generators and dead-time controllers are therefore important in guaranteeing the safe and efficient operations in half-bridge circuit power converters. These solutions are effective in addressing shoot-through and ringing and can thus decrease losses.

The presented DTCC design enhances the performance of half-bridge power converters. It uses a two-sided wide swing current source, a switched capacitor structure, and a particular signaling technique to generate precise delays between the required non-overlapping gate driving signals, and accurately drive a half-bridge circuit and avoid losses or excessive power consumption due to shoot trough, etc. Compared to other dead-time circuit solutions, our DTCC circuit has the key advantage of generating two asymmetric delays, the operating parameters of which are independent of the half-bridge circuit parameters, for the high side and the low side of the converter. Additionally, the presented solution allows to generate required long delays between the high-side and low-side driving signals, which is highly desirable in high voltage applications. Such design reduces the imperfections in the entire signal propagation process in the half-bridge converter to achieve lower power consumption and better signal quality. In Section II, we describe the main idea and advantages of the proposed dead-time structure. The circuit implementation is also discussed. In Section III, we detail the experimental results. In Section IV, we summarize our conclusions.

II. PROPOSED DEAD-TIME CIRCUIT

Cross-connected NAND/NOR gates and a chain of inverters in feedback loops are used in conventional dead-time circuits to generate non-overlapping signals with delays [41]. The propagation delay of these inverters provides the delays in the non-overlapping signals. This configuration of integrated circuits produces typical picosecond delays and is thus not useful in various power applications requiring long delays in the range of nanoseconds (e.g., high-voltage circuits, high currents, and highly reactive loads) [32].

A. Proposed Architecture

The proposed DTCC enables the generation of nanosecond delays and mitigates shoot-throughs at the same time. This property of the proposed DTCC decreases the power losses in power converters. Figure 3(a) shows the presented scheme. Specifically, the scheme comprises two-sided wide swing current sources (TS-WSCS) for linearly charging two capacitors (C_1 and C_2) on each side of the circuit. Each side of the circuit also has three switches for controlling the charging and discharging processes. Moreover, the right and left branches of the circuit are equipped with two Schmitt triggers (STs) with defined comparison hysteresis windows. These STs restrict the values of the generated delays between the two non-overlapping driving signals.

Figure 3 (b) shows the predefined state machine that reflects the originality of the proposed idea. Specifically, the figure illustrates the non-overlapping timing methodology for the low- and high sides of half-bridge converters. The states in this machine are change polarity "CP", close switch "CS", charge capacitors "CC", and Schmitt trigger "ST". The presented active dead-time circuit is controlled by a finite state machine

This article has been accepted for inclusion in a future issue of this journal. Content is final as presented, with the exception of pagination.

KARIMI *et al.*: ACTIVE DEAD-TIME CONTROL CIRCUIT WITH TIMING ELEMENTS

3

(FSM) to generate the required half-bridge control delays. The circuit operation based on the FSM is clarified according to Fig. 3 (b). The circuit operation is illustrated according to Fig. 3 (b). Given an operating high-side power switch (operating HS), the polarity of the signal at its output is supposed to change (CP HS) instantly when the deactivating signal arrives at its gate (deactivating HS). However, the process is time consuming because of the large parasitic capacitance of the HSPS. In meeting the required time, the Φ_2 signal should close the corresponding controlling switch before the LSPS is activated (CS LS). The TS-WSCS then charges the capacitor C_2 linearly (CC LS) to reach the upper bound of the utilized ST (ST LS). At this point, the HSPS is deactivated completely (deactivated HS). This process should generate t_{d2}. In Fig. 3 (b), the process is labeled as the "B" process. The activation of the LSPS (operating LS) is provided similar to "B" process which is named "A" process. This process should also generate the time required to completely deactivate the LSPS before the activation of the HSPS again. Figure 3 (c) presents the timing diagram, which includes four curves tagged by t_{d1}, t_{d2} and the different working states of the proposed DTCC [32].

The proposed DTCC approach offers the following benefits:

1- The amount of current delivered by the TS-WSCS, the values of the capacitors, and the comparison levels of STs determine the generated delay of the circuit. Adjusting these parameters thus helps obtain the long delays needed in high-voltage and power applications, including those requiring large parasitic capacitances (e.g., power switches).

2- To set the delays between non-overlapping signals independently, the proposed circuit generates different time delays t_{d1} and t_{d2}. Such capability facilitates the adjustment of the delays of the low- and high-side parts. In particular, the driving signals of the HSPS go through more stages (i.e., level shifter and gate driver) than those of the LSPS. Thus, ensuring the absence of any overlap between switch operations calls for a longer t_{d2} than t_{d1}.

3- The signals for arranging the capacitors and current source in the presented circuit are based on a predefined FSM. Specifically, this FSM is used to charge/discharge the capacitors and utilize/remove the current source and thereby produce a suitable dead time. This property reflects the originality of the presented circuit.

A gate driver with two independent inputs serves as the interface between the proposed DTCC and output stage of the half-bridge converter. This interface helps fulfill the practical operation of the proposed dead-time circuit for the half-bridge converter. Specifically, the gate driver receives non-overlapping signals from the proposed DTCC and then delivers them to the HSPS and LSPS. It also provides the power switches with an adequate amount of driving current from its supply.

B. Circuit Implementation

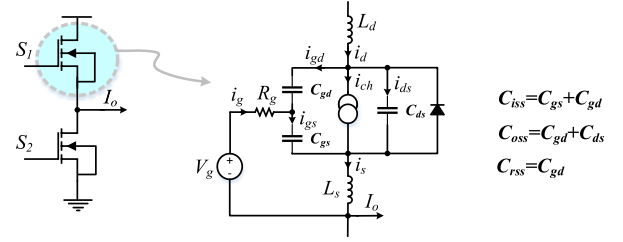Our dead-time circuit prototype chip fulfills the R-L load requirements of a standard high-voltage data bus [27], hav-

Fig. 1. Half-bridge output stage and equivalent circuit of power switch during operation.

TABLE I
ASPECT RATIOS OF TS-WSCS TRANSISTORS

	MP1, MP2	MP3	MP4 - MP7	MN1, MN2
W (µm)	10	5	10	0.4
L (µm)	0.35	0.35	0.35	5

ing $V_{IN} = 45V$ and driving a R-L load of R=100 Ω and L=150 μH with a half-bridge converter. The presented dead-time circuit prototype can provide high-side and low-side delays of 35 ns and 62 ns to such a half-bridge converter. The transistor-level implementation of the proposed DTCC is shown in Fig. 4 (a). The TS-WSCS supplies the charging current of capacitors C_1 and C_2. The sources are formed by nine MOSFETs (MP1–MP7 and MN1, MN2). MN1 and MN2 are two diode connected transistors that serve as current sources for respectively generating I_{in} and I_{bias}. MP1, MP2, and MP3 are used to bias the cascaded transistors MP4, MP5, MP6, and MP7. The following design strategies are considered to ensure that the TS-WSCS circuit functions:

1) Currents I_{bias} and I_{in} are set to be equal for MP1–MP7 to be in their saturation region.

2) The width of MP3 is set to half of that of MP1, MP2, and MP4–MP7. The setting should bias MP1, MP4, and MP6 properly in the active region.

3) Minimum gate lengths are adopted for MP1, MP4, and MP6 to maximize the frequency response.

The aspect ratios of the transistors used for the TS-WSCS are listed in Table I. A ramp signal is generated using the timing elements MN3–MN8 (i.e., transmission gates), C_1–C_2, and control signals ($\Phi_1 - \Phi_2$). Driven by Φ_1 and Φ_2, MN3–MN8 are utilized to linearly regulate the charging and discharging times of C_1 and C_2. The TS-WSCS circuit can be quickly turned on and off. Therefore, a 0.6 V offset resulting from the residual charges (Fig. 4 (a)) in C_1 and C_2 after one transition is added to the generated ramp signal at nodes 1 and 2 (Fig. 4 (a)). In this case, MN3 and MN6 are added to remove the residual charge and cancel the generated offset. The addition is possible if MN3 and MN6 are activated in phase with MN5 and MN8, respectively. The required delays are generated using two STs. In setting the STs' hysteresis windows, their reference voltages are adjusted to $V_{ref1} = 0.76$ V and $V_{ref2} = 1.74$ V. Following the adjustment, the STs can then generate a non-overlapping signal that provides enough dead-time to avoid shoot-throughs in the converter resulting from the ramp signals generated across the
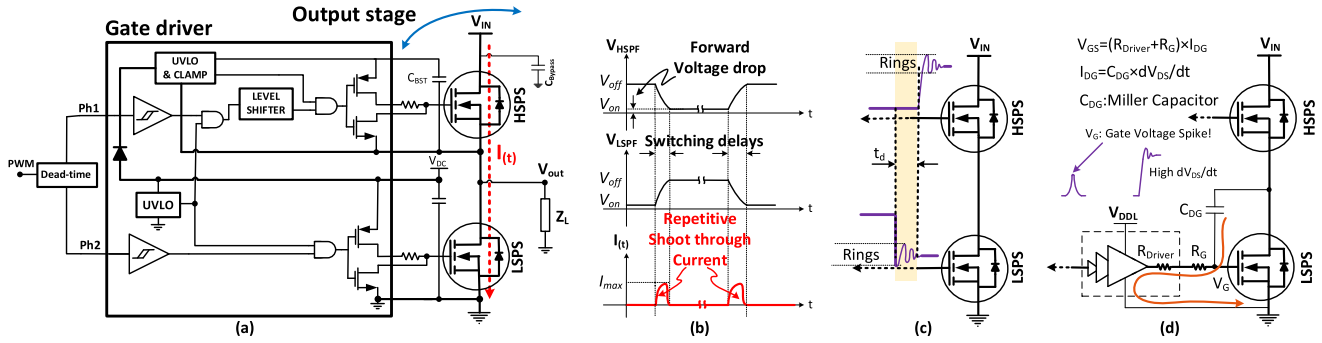
Fig. 2. Power converter and the different sources of shoot-through: (a) half-bridge circuit with simplified dead-time circuit, (b) impact of switching delays, (c) ringing effect due to the output parasitic capacitance (C_{oss}) of HSPS, and (d) Miller capacitor effect.

capacitors C_1 and C_2. Fig. 4 (a) shows that the ST circuits are surrounded by two boxes. Fig. 4 (b) illustrates the effect of the offset added to the ramp signals of node 1 with and without the addition of MN3 and MN6. The slope of the ramp signals decreases because of the added offset without the use of MN3 and MN6. The generated delay is thus 5 ns longer than expected.

The following equations are arranged to show the relation between the generated delays (t_{d1} and t_{d2}) and the circuit parameters. The equation for the capacitor is

$$i_c(t) = C \cdot \frac{dV_c(t)}{dt}, (t_0 \leq t \leq t_1) => \quad (1a)$$

$$i_c(t) \cdot dt = C \cdot dV_c(t), (V_0 < V_c(t) < V_1) \quad (1b)$$

Constant current is delivered to the capacitors. Hence, the following equation is obtained through the integration from t_0 to t_1 and from V_0 to V_1, with the upper and lower bounds of the integrals being ST reference voltages and their corresponding start and stop times:

$$\int_{t_0}^{t_1} i_c(t) \cdot dt = C \cdot \int_{V_0}^{V_1} dV_c(t) => \quad (2a)$$

$$I \times [t_1 - t_0] = C \times [V_C(t_1) - V_C(t_0)] => \quad (2b)$$

$$I \times [t_1 - t_0] = C \times [V_1 - V_0], \quad (2c)$$

where $V_C(t_0) = V_0 = 0$ as the capacitors are reset after each period and $t_0 = 0$ is the time at which the capacitors start charging at the beginning of each period. Assume that t_1 is the time at which the ramp signal (ramp = k·t, where k = I/C and "t" is the time) reaches the high level of the ST window. In this case, t_{d1} and t_{d2} can be expressed as

$$t_{d1} = (C_1/I_{C_1}) \times V_{ref2}, \quad (3a)$$

$$t_{d2} = (C_2/I_{C2}) \times V_{ref2}, \quad (3b)$$

where V_{ref2} is the trigger voltage of the STs located on each side of the TS-WSCS. The generated delays in the proposed DTCC rely on the values of the I_{C1} and I_{C2} currents (Fig. 4 (a)) that the TS-WSCS delivers to the capacitors. Given the relation between the output current and the values of I_{in} and I_{bias}, the operation of the proposed design against mismatch and process corners should be validated. Specifically, MN1 and MN2 (Fig. 4 (a)) that are used to adjust the biasing current should be made robust against process variations. The
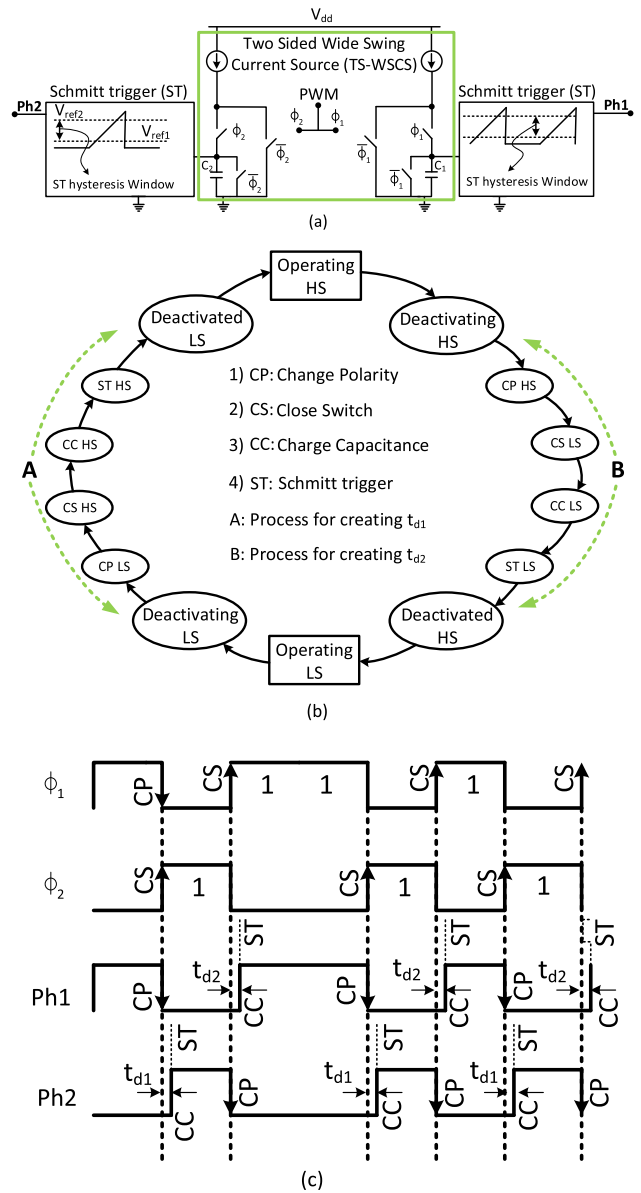

Fig. 3. Proposed dead-time control circuit: (a) simplified schematic, (b) state machine representation, and (c) timing diagram.

operations on both sides of the proposed DTCC during the generation of t_{d1} and t_{d2} are the same. A different t_d is due to the different parameter values on each side of the circuit. Therefore, the circuit is evaluated to be robust against process
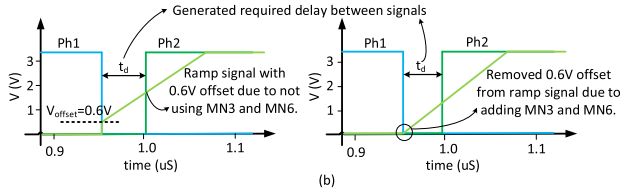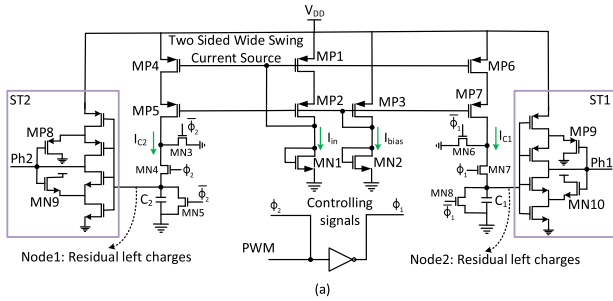
Fig. 4. (a) Transistor-level implementation of proposed DTCC, (b) added offset to the ramp signal with and without MN3 and MN6.
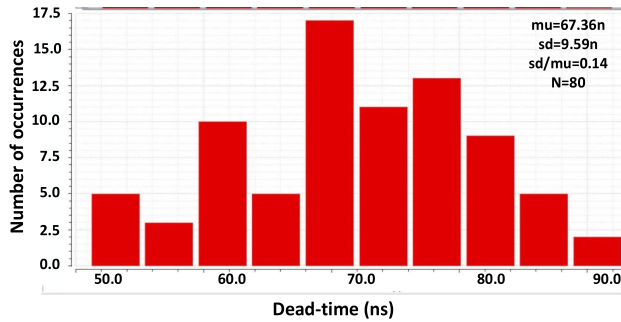

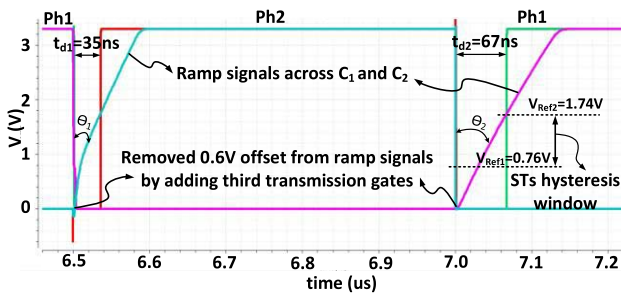Fig. 5. Evaluation of DTCC operation with a Monte-Carlo simulation.

Fig. 6. Simulated dead time between signals.

variations for one of the delays (i.e., t_{d2}). For the designed circuit of the typical case corner, i.e., typical NMOS and PMOS transistors and $V_{DD} = 3.3$V, the simulated dead-time value t_{d2} is 67 ns. A worst-case scenario is simulated to cope with process variations. In the AMS kit, "fast NMOS/fast PMOS" corresponds to "worst power" (WP) while "slow NMOS/slow PMOS" corresponds to "worst speed" (WS). In this study, we evaluate the operation of the proposed circuit in the WP and WS cases. The WP and WS cause process variations and are thus the worst conditions of component operations. The simulated dead-time values t_{d2} for the WP and WS cases are 50.0 and 90.0 ns, respectively. Obviously,
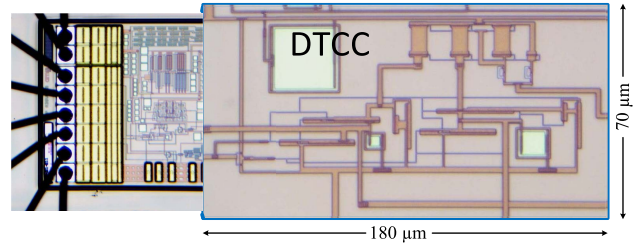

Fig. 7. Chip micrograph of fabricated DTCC in CMOS AMS 0.35 μm.

the WS case yields the longest dead-time while the WP has the shortest dead-time. In this work, the impact of the process variations on the performance of the proposed DTCC is studied using a Monte Carlo simulation. A supply voltage of $V_{DD} = 3.3$ V is set for the simulation. The results for t_{d2} are shown in Fig. 5. Specifically, the simulated t_{d2} shows a log-normal distribution with a variance of 0.14. The *average delay* of t_{d2} is 67.36 ns, and the standard deviation is 9.59 ns. This work aims for a robust design against process variations with the lowest standard deviation. Therefore, the dimensions of MN1 and MN2, which are responsible for biasing the circuit, should be increased. At the same time, the same aspect ratio "W/L" should be maintained. However, both tasks lead to a trade-off between the chip area and the sensitivity of the generated delay to process variations.

The impact of the parasitic inductance on the produced dead-time delays is examined through post-layout simulations. The relevant voltages, including the non-overlapping signals (Ph1, Ph2), and the ramp signal across capacitors (C_1 and C_2) are shown in Fig. 6. The figure also presents the parameters of $t_{d1} = 35$ ns, $t_{d2} = 67$ ns, $V_{ref2} = 1.74$ V, and $V_{ref1} = 0.76$ V. After the addition of the MN3 and MN6 transmission gates at high and low STs, the 0.6 V offset is effectively removed from the ramp signal. As observed in Fig. 6, the generated delays between the non-overlapping signals rely mainly on the slope of the ramp signals. Moreover, the hysteresis windows of the STs differ (as the capacitance of C_2 is relatively large, the slope of the ramp signals is slow). Therefore, the upper bound of the level shifter (V_{ref2}) on the corresponding side of C_2 meets the ramp signals later. The generated t_{d2} is thus longer than t_{d1}. The delays in the design could be set in other ways. For example, the amount of the current delivered to the capacitors can be set. Another option is to set the STs' hysteresis window parameters by the upper and lower bounds on the basis of the sizes of MP8, MP9, MN9, and MN10 in the design (Fig. 4 (a)).

In Fig. 6, Θ_1 and Θ_2 respectively denote the angles between the generated ramp signals and the falling edges of the non-overlapping signals. A ramp signal with a sharp slope yields a small angle. A small angle in this case results in a short dead-time because the ramp signal produced meets V_{ref2} of the corresponding ST early. At this point, the proposed DTCC is implemented to produce fixed t_{d1} and t_{d2} for a specific power converter. In the post-layout simulation, the proposed DTCC without PADs consumes 190 μW of power under no load conditions.

This article has been accepted for inclusion in a future issue of this journal. Content is final as presented, with the exception of pagination.

6

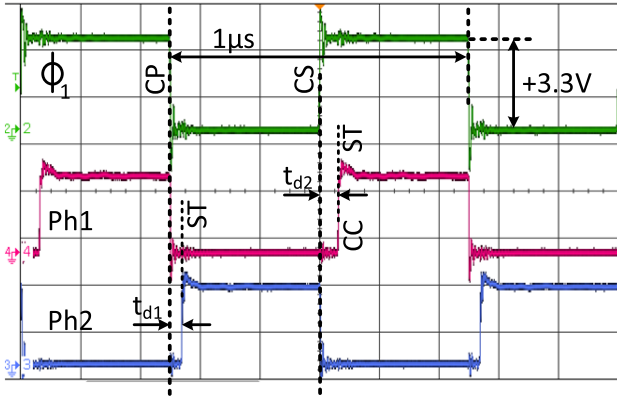IEEE TRANSACTIONS ON CIRCUITS AND SYSTEMS—I: REGULAR PAPERS

Fig. 8. Measured generated dead-time delays between non-overlapping signals.

III. MEASURED PERFORMANCE

We fabricate the proposed DTCC in AMS 0.35 μm CMOS. The micrograph of the integrated chip prototype is shown in Fig. 7. The proposed circuit occupies an area of 180 μm $\times$ 70 μm. The integrated DTCC is designed to generate t_{d1} = 35 ns and t_{d2} = 62 ns for the LSPS and HSPS, respectively, by using C_1 = 30fF and C_2 = 55fF. The lower and upper bounds for both STs on each side are 0.76 and 1.74 V, respectively. The delays meet the requirements of a projected power converter. The dead-time required by a power converter is contingent on the supply voltage (V_{IN}) and the current delivered to the load [3].

A. Results of DTCC Measurement

The measured non-overlapping signals produced by the DTCC prototype for a 1 MHz input square wave signal (Φ_1) and a supply voltage of 3.3 V are shown in Fig. 8. The figure also presents the four states (i.e., CP, ST, CS, and CC), delays (i.e., t_{d1} and t_{d2}), and signals (i.e., Ph1 and Ph2). A good agreement is reached between the experimental results and the projected timing diagram (Fig. 3 (c)). Moreover, the measured results agree well with the post-layout simulation results (Fig. 9 (a)). The measured and simulated delays with a precision of 0.01% and a supply voltage of 3.3 V are equal to t_{d1} = 35 ns for C_1 = 30fF. However, the measured results (62 ns) and simulated results (67 ns) present a difference in t_{d2} values for C_2 = 55fF. The results are presented in Fig. 9 (a). An increase in the supply voltage (V_{DD}) causes a decrease in the generated dead-time between non-overlapping signals according to a second-order function. In particular, the second-order effect is more distinct in the measurement than in the simulation (Fig. 9 (a)). An increase in V_{DD} boosts the V_{SG} values of MP1, MP4, and MP6 (Fig. 4 (a)). Moreover, the second-order function relates to the V_{SG} values of the MOSFETs biased in the saturation region and their drain current charge the capacitors C_1 and C_2. As presented in Equation (3), the I_{C1} and I_{C2} currents delivered to the capacitors are inversely related to the amount of generated dead-time (i.e., a large charging current results in a steep ramp signal, which in turn produces a short dead-time).

Therefore, the generated dead-time is associated with V_{DD} by a second-order descending curve. This work experimentally validates the operation of the proposed DTCC.

The validation is performed at different supply voltages (V_{DD}), over a frequency range of 10Hz-11MHz, and square input signals. Herein, t_{d1} and t_{d2} determine the frequency limitation (11 MHz) at different V_{DD}. The delays produced by the non-overlapping control signals are independent of the input signal frequency. Therefore, the frequency of the input signal can be increased up to $f_p \leq 1/(t_{d1} + t_{d2})$. Such a condition represents the extreme case in the proposed design. The effect of changes in V_{DD} on the maximum operating frequency is illustrated in Fig. 9 (b). The limitation is observed to only affect Ph2 of the non-overlapping signals generated. This result is due to the fact that an increase in frequency with a specific value of V_{DD} causes the values of t_{d1} and t_{d2} to be close. Therefore, Ph2 disappears while Ph1 is available. As mentioned previously, dead-time delay drops when V_{DD} increases. A reduced dead-time delay in turn increases the maximum operating frequency (Fig. 9 (b)).

The amplitudes of the undershoot and the overshoot ringing near the edge of the measured signals are -1.9 and $+1.1$ V, respectively (Fig. 10). In Fig. 10 (a), the red and blue curves mark Ph1 and Ph2, respectively. Ph1 reaches a high state when the ringing of its complimentary signal Ph2 becomes totally damped. The results reveal slight variations in the ringing observed in the non-overlapping parts of control signals which are provided for the gates of the HSPS and LSPS, respectively. The differences may be explained as follows: avoiding any overlap between the on-states of the superimposed complimentary switches of the power converter requires the generation of adequate dead-time (t_d) between the control signals. Figures 10 (a) and (b) respectively present the measured t_{d2} (62 ns) and t_{d1}(35 ns).

In Fig. 11, the measured power consumption of the proposed DTCC is shown as a function of the input frequency for different values of V_{DD}. The power indicated refers to static and dynamic power. Dynamic power is consumed by the charge and discharge of the capacitive load in the outputs of Ph1 and Ph2 of the fabricated chip connected to the half-bridge converter. Additional losses may also be incurred in the active PADs because of the internal CMOS stages used to buffer the I/O signals.

The capacitive load is estimated by measuring the slew rate of the non-overlapping signals generated when the DTCC is connected to the half-bridge converter, that is, C_L = $i_{dynamic}$/(slew rate). The slew rate is equal to 0.16 V/ns when the signals at the output of the DTCC range from 0.5 V to 3.0 V; the corresponding dynamic current is 2.5 mA. The circuit has two outputs, namely, Ph1 and Ph2. Dynamic current is consumed to drive the capacitive loads at the outputs of Ph1 and Ph2. Therefore, the total capacitive load of the DTCC is $C_{Lph1} + C_{Lph2}$ = 2.5mA/(0.16 $\times$ 10^9) = 15.62pF. Given the inputs of the gate driver having the same circuit, the capacitive load at each output is C_{Lph1} = C_{Lph2} = 7.81pF.

As shown in Fig. 11, the power consumption varies with frequency. This relationship is attributed to the switching losses of the MOSFETs that increase almost linearly with
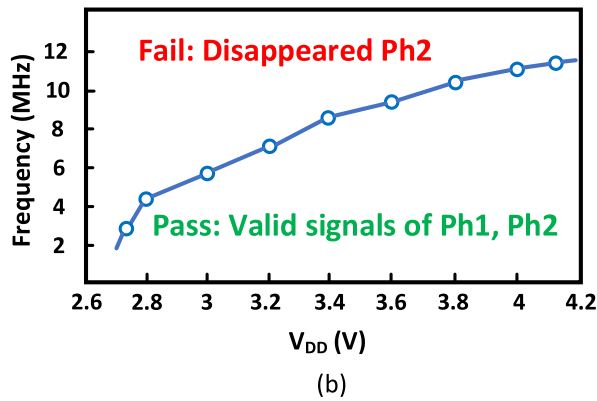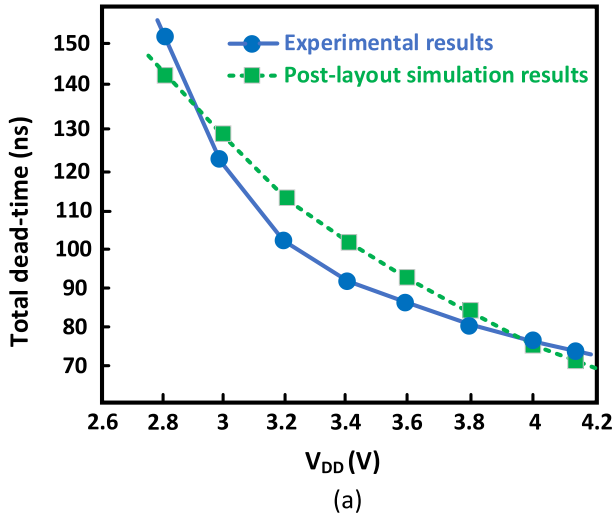
(a)

(b)

Fig. 9. Measured DTCC performances: (a) Comparison of the experimental and post-layout simulation results of the dead-time delays variation versus the power supply voltage V_{DD}. (b) The effect of V_{DD} on the maximum operating frequency of DTCC.

(a)

(b)

Fig. 10. Measured outputs of Ph1 and Ph2: (a) generated delay t_{d2} for the high side of half-bridge converter, (b) produced delay t_{d1} for the low side of half-bridge converter, and the amplitude of individual ringing at the edges of each phase.
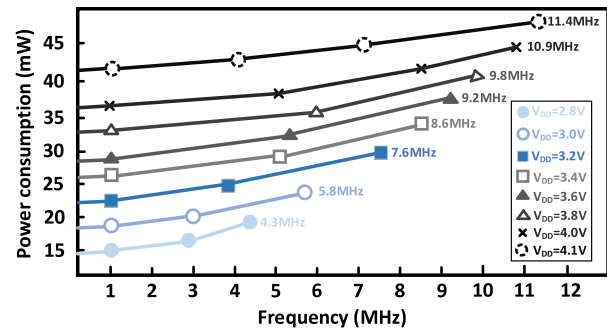
Fig. 11. Measured power consumption variation with respect to the input frequency for different values of V_{DD} for 7.81pF estimated capacitive load in each output of Ph1 and Ph2.

the operating frequency. In the proposed DTCC, the output currents I_{C1} and I_{C2} increase with V_{DD}. The same is true for the power consumption. Figure 11 also presents the variations of power consumption with the operating frequency given eight specific V_{DD} values. The maximum frequency of the circuit changes in line with V_{DD}. As the generated dead-time decreases with V_{DD}, the upper curve ($V_{DD} = 4.1$ V) achieves the highest maximum frequency with 11.4 MHz. As the frequency of the non-overlapping signal further increases and exceeds $1/(t_{d1}+t_{d2})$, Ph2 drops and then disappears completely. For a valid non-overlapping signal, the power consumption varies from 16.8 mW to 41 mW on the basis of V_{DD}, which can vary from 2.8 V to 4.1 V, and the operating frequency, which ranges from 100 kHz to 11.4 MHz.

B. Validation With Half-Bridge Circuit

The DTCC prototype is validated by implementing a half-bridge circuit with commercial components. The block diagram of the implemented half-bridge circuit with the fabricated DTCC is illustrated in Fig. 12. The eGaN HEMTs are driven by the LM5113 gate driver (Fig. 12). The power eGaN FET can work at voltages of up to 100 V and deliver currents

as high as 5 A to the load. Two independent high-side and low-side TTL logic inputs comprise the gate driver. These inputs are compatible with the fabricated DTCC chip. The LM5113 contains the required bootstrap (BST) diode. The commercial regulator MCP1703 supplies the gate driver with

Fig. 12. Block diagram of the test half-bridge circuit with the fabricated DTCC.

TABLE II
PERFORMANCE COMPARISON WITH PRIOR WORKS

	[42]	[48]	[51]	[52]	This work
Results	Meas.	Meas.	Meas.	Meas.	**Meas.**
Tech.(nm)	180	65	350	350	**350**
f_p (MHz)	10	10	10	0.1	**1**
t_d (ns)	0.125	1	Analog	200	**35 and 62**
I_O (mA)	200	120	600	500	**210**
V_{IN} (V)	12	5	3.6	250	**45**
ΔP_{loss} (%)	30.5	--	--	--	**32**
Effic.	81.2%	76.4%	--	77%@20W	**82%**

power for the half-bridge under-voltage lockout circuit, and the reverse recovery charge of the bootstrap diode. The minimum on-time of low-side transistor affects the value of the bootstrap capacitor; a value of over 0.1 μF is deemed satisfactory. Any power supply noise is removed by connecting two bypass capacitors in parallel between the input voltage (V_{IN}) and GND [41], [42].

The basic operations of the half-bridge circuit with inconvenient and convenient dead-time are respectively shown in Figs. 13 (a) and (b). Regardless of the operation, three critical power losses heat up the power switches and substantially affect the safety of the powe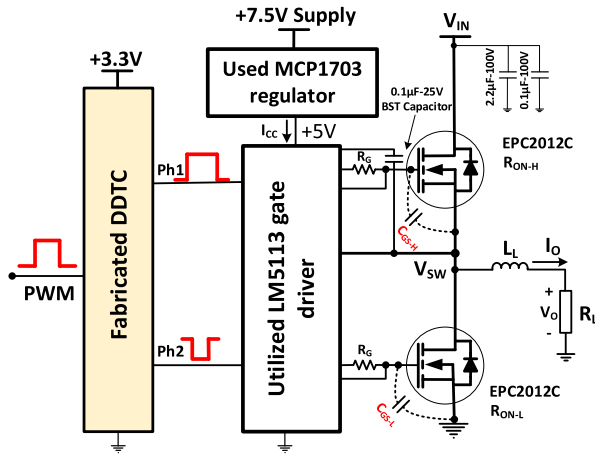r converter. These power losses depend on the overlap between the activation of the power switches. Hence, they can be minimized using a convenient DTCC. The dead-time dependent power losses (DDPLs) include conduction loss, switching delay loss, and shoot-through loss. These DDPLs are illustrated in Fig. 13 (a) with different colors and names (A, B, C, D, E, and F) [43]–[45]. Given a convenient amount of dead-time, losses A and B in the half-bridge circuit are totally eliminated, and the volumes of C–F are greatly minimized (Fig. 13(b)).

C. Power Loss Analysis

The total power losses in the designed power converter should be calculated on the basis of the measured parameters from the implemented converter [46], [47] to identify the effects of the proposed DTCC on the implemented half-bridge circuit.

The first DDPL is the conduction loss (Fig. 13). The conduction loss of the HSPS (P_{ON-H}) depends on the switch's on-resistance (R_{ON-H}) and the amount of current delivered to the load during the operation. The same description applies to the LSPS, that is, P_{ON-L} depends on R_{ON-L}. The second DDPL is the switching loss. The switching loss is due to the rise and fall times of the switching voltage V_{SW} (Fig. 13). The switching loss of the HSPS (P_{SW-H}) depends on the operating frequency of the power converter. It also relies on V_{IN} and I_O [32]. The third DDPL is the body diode loss (P_D), particularly in the Si or SiC MOSFETs. It is mainly caused by the reverse recovery of the inductor current (L_L current) by the body diode of the LSPS. P_D depends on the operating frequency of the converter and the forward voltage (V_D) of the LSPS' body diode [46]. For a half-bridge circuit, the gate charge loss (P_G) results from the gate charging of the power switches, and the gate driver loss is caused by gate charging
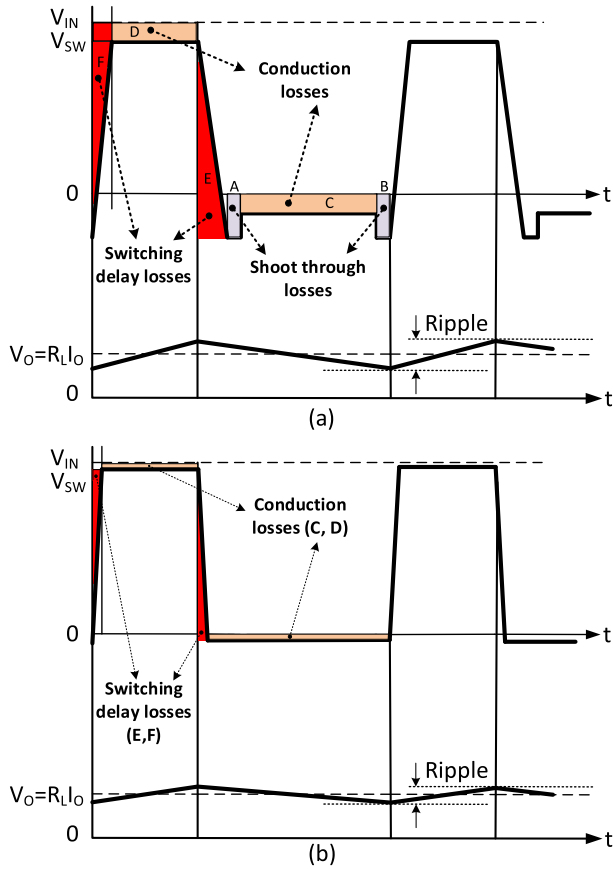

Fig. 13. Relevant waveforms of half-bridge circuit (a) with inconvenient amount of dead-time, showing the dead-time dependent losses of A, B, C, D, E, and F; and (b) with a convenient amount of dead-time, showing a significant dead-time dependent loss reduction.

5 V (Fig. 12). For the output stage of the half-bridge circuit, we utilize two eGaN HEMTs from EPC (EPC2012C), two freewheeling diodes (SDM03U40-7) placed in parallel with each power switch to reduce spikes in the inductive load, and a BST capacitor (C1005 $\times$ 5.1E104K050BC). The BST capacitor provides the gate charge for the HSPS, dc bias

This article has been accepted for inclusion in a future issue of this journal. Content is final as presented, with the exception of pagination.
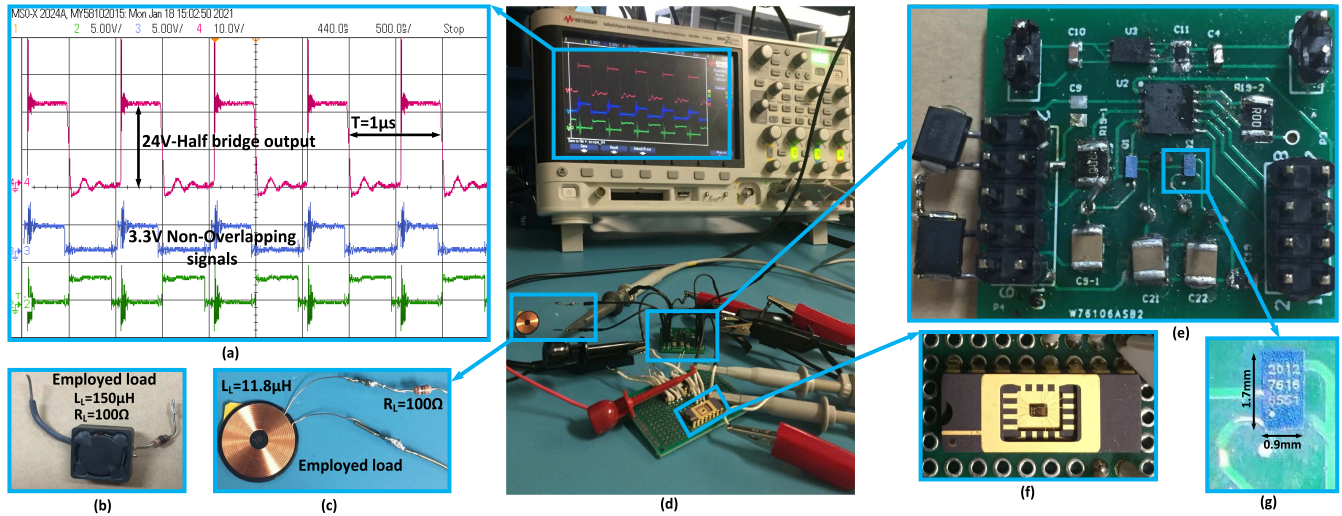
KARIMI *et al.*: ACTIVE DEAD-TIME CONTROL CIRCUIT WITH TIMING ELEMENTS

9

Fig. 14. Experimental setup of the half-bridge circuit. (a) Measured signals. (b) RL load with R = 100-Ω and L = 150-µH load. (c) RL load with R = 100-Ω and L = 11.8-µH load. (d) Test bench. (e) Custom printed circuit board. (f) Packaged fabricated chip. (g) Power GaN transistor.
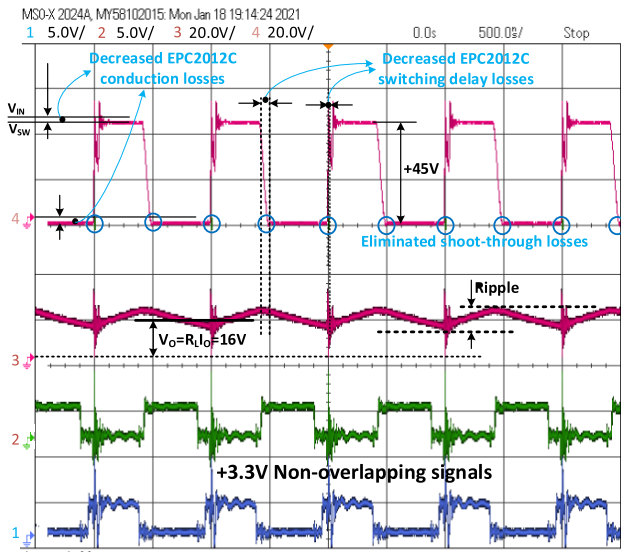

Fig. 15. Measured waveforms of the test half-bridge circuit with the fabricated DTCC circuit.

Fig. 16. Histogram of the calculated power losses of the test half-bridge circuit with and without the fabricated DTCC.

(P_{GD}). The loss of the fabricated DTCC (P_{DTCC}) must be added to the attained DDPLs, P_G, and P_{GD} losses to achieve the total power loss of the implemented half-bridge circuit [48]–[53].

The experimental setup for characterizing the implemented half-bridge circuit with the DTCC prototype is presented in Fig. 14. The required dead-time for a power converter depends on the values of the load and V_{IN}. In this work, we measure the performance of the half-bridge circuit with the fabricated DTCC under two conditions. In the first condition, the input voltage (V_{IN}) is 24 V, and the half-bridge circuit is configured to drive a 100 Ω resistor in series with a 11.8 µH inductor. In the second condition, V_{IN} is 45 V, and the load is a 100 Ω resistor in series with a 150 µH inductor. Figure 14 (a) shows a screenshot of the circuit in the first condition (V_{IN} = 24 V, R_L = 100 Ω, L_L = 11.8 µH) taken by

an oscilloscope. Meanwhile, Figs. 14 (b) and (c) present the output loads in the experimental setup for the two conditions. Figure 14 (d) illustrates the measurement setup. Figure 14 (e) shows the test's printed circuit board, including the half-bridge circuit. The size of the custom printed circuit board (PCB) used to characterize the half-bridge is 2.54 cm×3 cm and the size of the power switches are 1.7 mm × 0.9 mm. Figures 14 (f) and (g) respectively demonstrate the fabricated wire-bonded chip (DTCC) and one tiny power switch. Figure 15 plots the measured waveforms of the half-bridge circuit with the DTCC under the second condition. As shown in Figs. 14 (a) and 15, the DDPLs decrease significantly. The switching loss of the power switches is associated with the rise and fall times (t_r, t_f) of the V_{SW} (Fig. 13). The same is illustrated in Fig. 15. In the ON-state, the conduction loss of the power switches varies with the differences between the high levels of V_{IN} and V_{SW}. In the OFF-state, the conduction loss depends on the differences between the zero and low levels of V_{SW} (Fig. 13 (a)). As for the shoot-through loss, it is attributed to the A and B parts of the V_{SW} waveform

(Fig. 13 (a)). These parts are eliminated in the presented experimental results in Fig. 15.

D. Calculation of Power Losses

Figure 16 shows the histogram of the losses of the half-bridge circuit with and without the DTCC prototype. The blue and orange colors in the figure respectively represent the calculated losses of the half-bridge circuit with and without the fabricated DTCC. The power losses associated with the DDPLs of the half-bridge circuit with and without the DTCC prototype are 403.774 and 682.738 mW, respectively. This result implies a 40% improvement with the use of the proposed DTCC. The half-bridge circuit with the fabricated DTCC consumes 563.774 mW of total power; without the DTCC prototype, it consumes 834.538 mW. This result implies a 32% improvement in total power consumption when the proposed DTCC is utilized.

The maximum operating temperatures of the sensitive devices with and without the proposed DTCC are calculated. The results highlight the significance of the improvement of the power losses in the operation of the components of the half-bridge circuit. Figure 16 shows that the highest power loss corresponds to the switching loss of the HSPS (P_{SW}). The total power losses of the HSPS (i.e., $P_{ON-H} + P_{SW}$) with and without the proposed DTCC are 663.558 and 404.11 mW, respectively. According to the equations in [48], [49] and the specifications of EPC2012C, the calculated operating temperatures of the HSPS with (4a) and without (4b) the DTCC are

$$T_{Ja} = 404.11\text{mW} \times 85°\text{C/W} + 85°\text{C} = 119.3°\text{C} \quad (4a)$$
$$T_{Jb} = 663.558\text{mW} \times 85°\text{C/W} + 85°\text{C} = 141.4°\text{C} \quad (4b)$$

The calculated T_{Ja} and T_{Jb} remain below the absolute maximum rating of $T_J = 150 °C$ of EPC2012C. Nonetheless, the 22.1 °C improvement in the maximum temperature greatly enhances the safety of the half-bridge circuit.

Table II presents the measured performance of the half-bridge circuit with the proposed DTCC. The switching frequency (f_p), dead-time delay (t_d), output current (I_O), input voltage (V_{IN}), technology (Tech.), total loss improvement (ΔP_{loss}), and efficiency are compared with the reported measurement (Meas.) results of other solutions. The proposed DTCC circuit obviously provides the low and high sides of the half-bridge circuit with independent dead-time delays of 35 and 62 ns, respectively. These dead-times are robust and able to reduce the dependent losses of the half-bridge circuit by 40%. They also enhance the total power consumption by 32%. Meanwhile, the losses greatly decrease the maximum operating temperature of the half-bridge circuit. With the application of the proposed DTCC, the maximum operating temperature is considerably improved, thereby boosting the safety of the half-bridge circuit. A convenient dead-time can decrease the values of t_r, t_f, and the average delivered current. However, the values of V_{IN} and the operating frequency are fixed. That is why the amount of improvement of switching loss is limited.

IV. Conclusion

This study puts forward a circuit for generating dead-time delays to realize the proper non-overlapping operation of power converters. In traditional dead-time circuits, logic gates and inverters are used to create delays. Such scheme is prone to variations and limitations. By contrast, the proposed DTCC uses timing elements that integrate precise capacitors and current sources. The proposed DTCC can produce relatively long and independent time delays for HSPS and LSPS. The generated delays between the non-overlapping control signals meet the general requirements of half-bridge power converters. The proposed DTCC occupies a silicon area of 70 μm $\times$ 180 μm. It is validated using a test half-bridge circuit supplied at 45 V and 1 MHz. The half-bridge circuit is implemented with discrete off-the-shelf components. The effects of the proposed DTCC on the losses of the test converter are evaluated herein. The results show that the proposed DTCC improves the dead-time dependent converter losses by 40%. The measured performance of the presented DTCC is also compared with that of previous solutions.

Acknowledgment

References

[1] T. U. Kim, H. Y. Kim, and H. Y. Choi, "Design of TDMA noise-immune DC-DC boost converter with dead-time controller for AMOLED displays," in *Proc. 35th Int. Tech. Conf. Circuits/Syst., Comput. Commun. (ITC-CSCC)*, Nagoya, Japan, 2020, pp. 456–459.

[2] P. Y. Wang *et al.*, "A 10 MHz GaN driver IC with bang-bang dead-time control for synchronous rectifier buck converter," in *Proc. IEEE Energy Convers. Congr. Exposit. (ECCE)*, Detroit, MI, USA, Oct. 2020, pp. 3776–3781.

[3] P. K. Chiu, P. Y. Wang, S. T. Li, C. J. Chen, and Y. T. Chen, "A GaN driver IC with novel highly digitally adaptive dead-time control for synchronous rectifier buck converter," in *Proc. IEEE Energy Convers. Congr. Exposit. (ECCE)*, Detroit, MI, USA, Oct. 2020, pp. 3788–3792.

[4] V. Valente, C. Eder, N. Donaldson, and A. Demosthenous, "A high-power CMOS class-D amplifier for inductive-link medical transmitters," *IEEE Trans. Power Electron.*, vol. 30, no. 8, pp. 4477–4488, Aug. 2015.

[5] Z. Chen, Y.-T. Wong, T.-S. Yim, and W.-H. Ki, "A 12 A 50 V half-bridge gate driver for enhancement-mode GaN HEMTs with digital dead-time correction," in *Proc. IEEE Int. Symp. Circuits Syst. (ISCAS)*, Lisbon, Portugal, May 2015, pp. 1750–1753.

[6] H. Cetinkaya, A. Zeki, A. Girgin, E. D. Karabeyoglu, and T. C. Karalar, "A 1.6 GHz non-overlap clock generation with differential clock driver and clock level shifters for GS/s sampling rate pipeline ADCs," in *Proc. 25th IEEE Int. Conf. Electron., Circuits Syst. (ICECS)*, Bordeaux, France, Dec. 2018, pp. 277–280.

[7] S. N. Easwaran, M. Mollat, D. Sreedharan, S. Camdzic, S. V. Kashvap, and R. Weigel, "3A fault tolerant low side driver circuit design using design FMEA for automotive applications," in *Proc. 17th IEEE Int. New Circuits Syst. Conf. (NEWCAS)*, Munich, Germany, Jun. 2019, pp. 1–4.

[8] S. N. Easwaran, S. Chellamuthu, S. K. Venugopal, and R. Weigel, "Voltage and current selector-based biasing topology for multiple supply voltage circuits," *IEEE Trans. Circuits Syst. II, Exp. Briefs*, vol. 65, no. 1, pp. 11–15, Jan. 2018.

[9] S. Buetow, R. Herzer, N. Burani, R. Bittner, and M. Kujath, "New compact automotive SiC-sixpack converter system with stacked 3D-gate driver," in *Proc. 31st Int. Symp. Power Semiconductor Devices ICs (ISPSD)*, Shanghai, China, May 2019, pp. 235–238.

[10] S. Piepenbreier *et al.*, "Analysis of a multiphase multi-star PMSM drive system with SiC-based inverter for an automotive application," in *Proc. PCIM Eur.*, Jun. 2018, pp. 1–10.

This article has been accepted for inclusion in a future issue of this journal. Content is final as presented, with the exception of pagination.

KARIMI *et al.*: ACTIVE DEAD-TIME CONTROL CIRCUIT WITH TIMING ELEMENTS

11

[11] M. Karimi, H. Jouaicha, F. Lellouche, P.-A. Bouchard, M. Sawan, and B. Gosselin, "A 6.78-MHz robust WPT system with inductive link bandwidth extended for cm-sized implantable medical devices," in *Proc. 42nd Annu. Int. Conf. IEEE Eng. Med. Biol. Soc. (EMBC)*, Montreal, QC, Canada, Jul. 2020, pp. 4196–4199.

[12] J. A. Hora, A. C. Arellano, X. Zhu, and E. Dutkiewicz, "Design of buck converter with dead-time control and automatic power-down system for WSN application," in *Proc. IEEE Wireless Power Transf. Conf. (WPTC)*, London, U.K., Jun. 2019, pp. 582–586.

[13] S. A. Mirbozorgi, H. Bahrami, M. Sawan, L. A. Rusch, and B. Gosselin, "A single-chip full-duplex high speed transceiver for multi-site stimulating and recording neural implants," *IEEE Trans. Biomed. Circuits Syst.*, vol. 10, no. 3, pp. 643–653, Jun. 2016.

[14] M. Faizollah *et al.*, "A low-power generic biostimulator with arbitrary pulse shape based on a central control core," *IEICE Electron. Exp.*, vol. 30, no. 7, pp. 3964–3975, Jul. 2015.

[15] D. M. V. D. Sype, A. P. M. V. D. Bossche, J. Maes, and J. A. Melkebeek, "Gate-drive circuit for zero-voltage-switching half-and full-bridge converters," *IEEE Trans. Ind. Appl.*, vol. 38, no. 5, pp. 1380–1388, Sep. 2002.

[16] M. L. Beye *et al.*, "Active gate driver and management of the switching speed of GaN transistors during turn-on and turn-off," *Electronics*, vol. 10, no. 106, pp. 1–14, 2021.

[17] S. K. Roy and K. Basu, "Analytical model to study turn-off soft switching dynamics of SiC MOSFET in a half-bridge configuration," *IEEE Trans. Power Electron.*, early access, Apr. 12, 2021, doi: 10.1109/TPEL.2021.3072329.

[18] J.-I. Baek, C.-E. Kim, J.-B. Lee, H.-S. Youn, and G.-W. Moon, "A simple SR gate driving circuit with reduced gate driving loss for phase-shifted full-bridge converter," *IEEE Trans. Power Electron.*, vol. 33, no. 11, pp. 9310–9317, Nov. 2018.

[19] Y.-D. Lee, D. Kim, S.-H. Choi, G.-W. Moon, and C.-E. Kim, "New bridgeless power factor correction converter with simple gate driving circuit and high efficiency for server power applications," *IEEE Trans. Power Electron.*, vol. 35, no. 12, pp. 13148–13156, Dec. 2020.

[20] M. R. Ahmed, R. Todd, and A. J. Forsyth, "Predicting SiC MOSFET behavior under hard-switching, soft-switching, and false turn-on conditions," *IEEE Trans. Ind. Electron.*, vol. 64, no. 11, pp. 9001–9011, Nov. 2017.

[21] J. Wang, H. S. H. Chung, and R. T. H. Li, "Characterization and experimental assessment of the effects of parasitic elements on the MOSFET switching performance," *IEEE Trans. Power Electron.*, vol. 28, no. 1, pp. 573–590, Jan. 2013.

[22] N. Oswald, P. Anthony, N. McNeill, and B. H. Stark, "An experimental investigation of the tradeoff between switching losses and EMI generation with hard-switched all-Si, Si-SiC, and all-SiC device combinations," *IEEE Trans. Power Electron.*, vol. 29, no. 5, pp. 2393–2407, May 2014.

[23] M. D. Bellar, T. S. Wu, A. Tchamdjou, J. Mahdavi, and M. Ehsani, "A review of soft-switched DC-AC converters," *IEEE Trans. Ind. Appl.*, vol. 34, no. 4, pp. 847–860, Jul. 1998.

[24] C. Liu, A. Johnson, and J.-S. Lai, "A novel three-phase high-power soft-switched DC/DC converter for low-voltage fuel cell applications," *IEEE Trans. Ind. Appl.*, vol. 41, no. 6, pp. 1691–1697, Nov./Dec. 2005.

[25] B. Sun, Z. Zhang, and M. A. E. Andersen, "A comparison review of the resonant gate driver in the silicon MOSFET and the GaN transistor application," *IEEE Trans. Ind. Appl.*, vol. 55, no. 6, pp. 7776–7786, Nov. 2019.

[26] A. Seidel and B. Wicht, "Integrated gate drivers based on high-voltage energy storing for GaN transistors," *IEEE J. Solid-State Circuits*, vol. 53, no. 12, pp. 3446–3454, Dec. 2018.

[27] *SN65HVDA100-Q1 LIN Physical Interface*, Texas Instruments, Dallas, TX, USA, Nov. 2011, Accessed: Jul. 2015.

[28] M. Karimi, M. Ali, A. Hassan, M. Sawan, and B. Gosselin, "A wide-range reconfigurable deadtime and delay element for optimal-power conversion," in *Proc. 19th IEEE Int. New Circuits Syst. Conf. (NEWCAS)*, Jun. 2021, pp. 1–4.

[29] O. P. Hari and A. K. Mai, "Low power and area efficient implementation of N-phase non overlapping clock generator using GDI technique," in *Proc. 3rd Int. Conf. Electron. Comput. Technol.*, Kanyakumari, India, Apr. 2011, pp. 123–127.

[30] S. M. Vazgen, "Adjustable low-power non-overlap clock generator for switched-capacitor circuits," in *Proc. 2nd Int. Conf. Elect., Electron. Comput. Eng. (IcETRAN)*, 2015, pp. 1–4.

[31] S. A. Zahrai, N. L. Dortz, and M. Onabajo, "Design of clock generation circuitry for high-speed subranging time-interleaved ADCs," in *Proc. IEEE Int. Symp. Circuits Syst. (ISCAS)*, Baltimore, MD, USA, May 2017, pp. 1–4.

[32] M. Karimi *et al.*, "A versatile non-overlapping signal generator for efficient power-converters operation," in *Proc. IEEE Int. Symp. Circuits Syst. (ISCAS)*, Seville, Spain, Oct. 2020, pp. 1–5.

[33] L. Balogh, "Fundamentals of MOSFET and IGBT gate driver circuits," Texas Instrum. Incorporated, Dallas, TX, USA, Tech. Rep. SLUA618, SLUP169, Mar. 2017, Accessed: April 2002.

[34] S. Zhang and X. Wu, "Low common mode noise half-bridge LLC DC–DC converter with an asymmetric center tapped rectifier," *IEEE Trans. Power Electron.*, vol. 34, no. 2, pp. 1032–1037, Feb. 2019.

[35] D. Li, F. Xia, J. Luo, and A. Yakovlev, "Modelling reversion loss and shoot-through current in switched-capacitor DC–DC converters with Petri nets," in *Proc. 29th Int. Symp. Power Timing Model., Optim. Simul. (PATMOS)*, Rhodes, Greece, Jul. 2019, pp. 69–74.

[36] I. Roasto, D. Vinnikov, J. Zakis, and O. Husev, "New shoot-through control methods for qZSI-based DC/DC converters," *IEEE Trans. Ind. Informat.*, vol. 9, no. 2, pp. 640–647, May 2013.

[37] L. Ibarra, P. Ponce, and A. Molina, "An adjustable sensorless shoot-through protection for H-bridges," in *Proc. 44th Annu. Conf. IEEE Ind. Electron. Soc. (IECON)*, Washington, DC, USA, Oct. 2018, pp. 379–384.

[38] S. T. Li *et al.*, "A 10 MHz GaN driver with gate ringing suppression and active bootstrap control," in *Proc. IEEE Workshop Wide Bandgap Power Devices Appl. Asia (WiPDA Asia)*, Taipei, Taiwan, May 2019, pp. 1–4.

[39] A. Seidel and B. Wicht, "A fully integrated three-level 11.6 nC gate driver supporting GaN gate injection transistors," in *IEEE Int. Solid-State Circuits Conf. (ISSCC) Dig. Tech. Papers*, San Francisco, CA, USA, Feb. 2018, pp. 384–386.

[40] N. Ly, N. Aimaier, A. H. Alameh, Y. Blaquiere, G. Cowan, and N. G. Constantin, "A high voltage multi-purpose on-the-fly reconfigurable half-bridge gate driver for GaN HEMTs in 0.18-μm HV SOI CMOS technology," in *Proc. 18th IEEE Int. New Circuits Syst. Conf. (NEWCAS)*, Montreal, QC, Canada, Jun. 2020, pp. 178–181.

[41] S. Yin, K. J. Tseng, C. F. Tong, R. Simanjorang, C. J. Gajanayake, and A. K. Gupta, "A novel gate assisted circuit to reduce switching loss and eliminate shoot-through in SiC half bridge configuration," in *Proc. IEEE Appl. Power Electron. Conf. Exposit. (APEC)*, Long Beach, CA, USA, Mar. 2016, pp. 3058–3064.

[42] J. Wittmann, A. Barner, T. Rosahl, and B. Wicht, "An 18 V input 10 MHz buck converter with 125 ps mixed-signal dead time control," *IEEE J. Solid-State Circuits*, vol. 51, no. 7, pp. 1705–1715, Jul. 2016.

[43] M. Karimi *et al.*, "A 1.99-ns 0.5-pJ wide frequency range level shifter with closed-loop negative feedback," in *Proc. 18th IEEE Int. New Circuits Syst. Conf. (NEWCAS)*, Montreal, QC, Canada, Jun. 2020, pp. 174–177.

[44] H. Wen, Y. Zhang, D. Jiao, and J.-S. Lai, "A new method of switching loss evaluation for GaN HEMTs in half-bridge configuration," in *Proc. IEEE Appl. Power Electron. Conf. Exposit. (APEC)*, New Orleans, LA, USA, Mar. 2020, pp. 647–651.

[45] W. Lee, D. Han, C. Morris, and B. Sarlioglu, "Minimizing switching losses in high switching frequency GaN-based synchronous buck converter with zero-voltage resonant-transition switching," in *Proc. 9th Int. Conf. Power Electron. ECCE Asia (ICPE-ECCE Asia)*, Seoul, South Korea, Jun. 2015, pp. 233–239.

[46] R. Hou, Y. Shen, H. Zhao, H. Hu, J. Lu, and T. Long, "Power loss characterization and modeling for GaN-based hard-switching half-bridges considering dynamic on-state resistance," *IEEE Trans. Transport. Electrific.*, vol. 6, no. 2, pp. 540–553, Jun. 2020.

[47] A. Ayachit and M. K. Kazimierczuk, "Averaged small-signal model of PWM DC-DC converters in CCM including switching power loss," *IEEE Trans. Circuits Syst. II, Exp. Briefs*, vol. 66, no. 2, pp. 262–266, Feb. 2019.

[48] G. Maderbacher *et al.*, "Automatic dead-time optimization in a high frequency DC–DC buck converter in 65 nm CMOS," in *Proc. ESSCIRC*, 2011, pp. 1919–1922. [Online]. Available: https://www.scribd.com/document/430695297/power-loss-appli-e-pdf

[49] M. Choi and D.-K. Jeong, "A 92.8%-peak-efficiency 60 A 48 V-to-1 V 3-level half-bridge DC–DC converter with balanced voltage on a flying capacitor," in *IEEE Int. Solid-State Circuits Conf. (ISSCC) Dig. Tech. Papers*, San Francisco, CA, USA, Feb. 2020, pp. 296–298.

[50] "Calculation of power loss," ROHM Semicond., Kyoto, Japan, Tech. Rep. AEK59-D1-0065-2, 2016.

This article has been accepted for inclusion in a future issue of this journal. Content is final as presented, with the exception of pagination.

12   IEEE TRANSACTIONS ON CIRCUITS AND SYSTEMS—I: REGULAR PAPERS

[51] W. Yan, C. Pi, W. Li, and R. Liu, "Dynamic dead-time controller for synchronous buck DC-DC converters," *Electron. Lett.*, vol. 46, no. 2, pp. 164–165, Jan. 2010.

[52] R. Grezaud, F. Ayel, N. Rouger, and J. Crebier, "A gate driver with integrated deadtime controller," *IEEE Trans. Power Electron.*, vol. 31, no. 12, pp. 8409–8421, Dec. 2016.

[53] M. Karimi, M. Ali, A. Hassan, M. Sawan, and B. Gosselin, "A reconfigurable single-supply multiple-level down-shifter for system-on-chip applications," in *Proc. IEEE Int. Symp. Circuits Syst. (ISCAS)*, May 2021, pp. 1–5.

[54] T. Y. Man, P. K. T. Mok, and M. Chan, "An auto-selectable-frequency pulse-width modulator for buck converters with improved light-load efficiency," in *IEEE Int. Solid-State Circuits Conf. (ISSCC) Dig. Tech. Papers*, Feb. 2008, pp. 440–626.

Mousa Karimi (Member, IEEE) received the B.Sc. degree in electrical engineering from Azad University (Boushehr Branch). He was with the Research Laboratory for Integrated Circuits and Systems (ICAS), Faculty of Electrical Engineering, K. N. Toosi University of Technology, Tehran, Iran, where he has done his master thesis on wireless interfacing design for bidirectional data communication with implanted microsystems and wireless power transmission (WPT) to implanted devices. He is currently with the Biomedical Microsystems Laboratory, Laval University, Quebec City, QC, Canada. His research interests include implantable microsystems, analog/digital/mixed-mode integrated circuits, wireless neural interfacing, and high voltage power converters design. He received the Mitacs Scholarship for collaboration with ULaval-MITACS-NSERC/CRD as his Ph.D. project. The results of his research presented in IEEE BioCAS, IEEE ISCAS, IEEE EMBC, and IEEE NEWCAS conferences. He is an Active Reviewer for many IEEE conferences, including the IEEE BioCAS, IEEE ISCAS, IEEE NEWCS, and IEEE EMBC conferences.

Mohamed Ali (Member, IEEE) received the B.Sc. degree in electronics from the Faculty of Electronics Engineering, Menoufia University, Egypt, in 2005, the M.Sc. degree in electronics and communication engineering from Ain Shams University, Egypt, in 2011, and the Ph.D. degree in electronics and communication engineering from Ain Shams University, jointly with the Polytechnique Montréal, Montreal, QC, Canada, in 2017. He joined the Polytechnique Montréal as a Research Intern from 2015 to 2017 as a part of his Ph.D. program. Since 2007, he has been with the Microelectronics Department, Electronics Research Institute, Giza, Egypt. He is currently a Post-Doctoral Fellow with the Department of Electrical Engineering, Polytechnique Montréal. His current research interests include analog, RF, and mixed-signal design.

Ahmad Hassan (Member, IEEE) received the Ph.D. degree in electrical engineering from Polytechnique Montreal, QC, Canada, in 2019. He currently holds a postdoctoral position with the Polystim Neurotechnologies Laboratory, Ecole Polytechnique de Montreal, Montreal. His research interests include high temperature microelectronics, including design and implementation of wireless power and data transmission systems dedicated for harsh environment applications.

Mohamad Sawan (Fellow, IEEE) received the Ph.D. degree in electrical engineering from Sherbrooke University, Canada, in 1990. From 1991 to 2019, he was leading Microsystems Strategic Alliance of Quebec. He is currently the Chair Professor, the Founder, and the Director of the Center for Biomedical Research and Innovation (CenBRAIN), Westlake University, Hangzhou, China. He is also an Emeritus Professor of microelectronics and biomedical engineering and the Founder and the Director of the Polystim Neurotech Laboratory, Polytechnique Montréal. He supervised the thesis of more than 100 master and 50 Ph.D. students. He published more than 800 peer reviewed articles. He was awarded 12 patents and 11 other patents are pending. He is a fellow of the Canadian Academy of Engineering and the Engineering Institute of Canada, and the Officer of the Quebec's National Order. He received several awards, among them the Queen Elizabeth II Golden Jubilee Medal, the Shanghai International Collaboration Award, the Bombardier Award for technology transfer, the Jacques-Rousseau Award for achieved results in multidisciplinary research activities, the Medal of Merit from the President of Lebanon for his outstanding contributions, and the Barbara Turnbull Award for spinal cord research in Canada. From 2000 to 2019, he was the Founder and the Chair of the IEEE-Solid State Circuits Society Montreal Chapter. Since 2019, he has been the Vice President of the publications of the IEEE CAS Society and the Founder and the Co-Founder of several international IEEE conferences, such as NEWCAS, BIOCAS, ICECS, and LSC. From 2016 to 2019, he was the Co-Founder and the Editor-in-Chief of the IEEE TRANSACTIONS ON BIOMEDICAL CIRCUITS AND SYSTEMS.

Benoit Gosselin (Member, IEEE) received the Ph.D. degree in electrical engineering from the École Polytechnique de Montréal in 2009. He was an NSERC Post-Doctoral Fellow with the Georgia Institute of Technology in 2010. He is currently a Full Professor with the Department of Electrical and Computer Engineering, Université Laval, where he also holds the Canada Research Chair in smart biomedical microsystems. His significant contribution to biomedical microsystems research led to commercializing the first wireless electro-optic bioimplant to study the development of brain diseases in freely behaving animal models by Doric Lenses Inc. His research interests include wireless microsystems for brain–computer interfaces, analog/mixed-mode and RF integrated circuits for neural engineering, interface circuits of implantable sensors/actuators, and point-of-care diagnostic microsystems for personalized healthcare. He is a fellow of the Canadian Academy of Engineering. He has received several awards, including the prestigious NSERC Brockhouse Canada Prize and the Prix Génie Innovation of the Quebec Professional Engineering Association OIQ. He was the Program Chair of the EMBC 2020, the first virtual EMBC in response to the COVID-19 pandemic. He is the Chair and the Founder of the IEEE CAS/EMB Quebec Chapter (the 2015 Best New Chapter Award). He is an Associate Editor of the IEEE TRANSACTIONS ON BIOMEDICAL CIRCUITS AND SYSTEMS. He served on the committees for several international IEEE conferences, including BIOCAS, NEWCAS, EMBC, LSC, and ISCAS.